Nanoscale characteristics of practical $LiFePO_4$ materials - effects on electrical, magnetic and electrochemical properties

Yin Zhang [a, b, d], Jose A. Alarco [a,*], Jawahar Y. Nerkar [a], Adam S. Best [b], Graeme A. Snook [c], and Peter C. Talbot [a]

[a] *Institute for Future Environments and Science and Engineering Faculty, Queensland University of Technology (QUT), Brisbane, QLD 4001 Australia.*

[b] *CSIRO Manufacturing, Private Bag 10, Clayton South, Victoria 3169, Australia.*

[c] *CSIRO Mineral Resources, Private Bag 10, Clayton South, Victoria 3169, Australia.*

[d] *CRRC Qingdao Sifang Rolling Stock Research Institute Co., Ltd., Qingdao 266031, China.*

Abstract

$LiFePO_4$ (LFP) is one of the important commercial battery materials, as such, many efforts have been made to understand its electrical and ionic conductivities and electrochemical properties. In this study, we have investigated electrochemical, electrical and magnetic properties of carbon coated LFP down to cryogenic temperatures. The fact that the practical material really consists of a core-shell structure with a shell of delithiated material and carbon coating determines the measured properties, which are often mistakenly attributed to pure LFP core behaviour. An electronic resistivity drop (11±0.5% based on the resistivity at room temperature), preceded by a gradual increase feature between 100-30 K, was observed when the temperature was below the Néel temperature at low applied currents, indicating a likely interaction between the magnetic configuration of the core LFP and electronic transport mechanisms. Metallic Fe_3P was precipitated on the samples surfaces after annealing at high temperature in Argon. The existence of Fe_3P was found to significantly improve the electronic conductivity but it took a toll on the electrochemical performance.

Keywords: Lithium iron phosphate, electronic conductivity, surface characterization, magnetic property

1. Introduction

$LiFePO_4$ (LFP) has been considered as one of the promising cathode materials for Lithium-ion batteries (LIB) since the original work of Goodenough et al. [1], due to its good chemical stability, competitive electrochemical properties, environmental friendliness and relative low cost. However, its high-rate application is limited by its low electrical ($\sim 10^{-9}$ S/cm) and ionic conductivities (10^{-13} to 10^{-16} cm ^{2}/s) [2, 3]. Therefore, modifications, such as particle size reduction [4], conductive surface coatings [5, 6], aliovalent doping [7-9] and composite electrode preparation [10, 11], have been extensively investigated to improve the conductivity of the modified LFP. Conductive carbon coating, as an efficient and low-cost modification method, has been widely used in the commercial production of LFP. Studies show that the electrical conductivity can be increased in the order of $\sim 10^6$ times with small amount of carbon coating (~ 2 w.t. %), also improving substantially the overall electrochemical utilization of the LFP battery material [12-14].

Crystalline LFP has an orthorhombic lattice structure with space group Pnma [15]. The oxygen ions in the ordered olivine structure form strong covalent bonds with phosphorous ions. The PO_4^{3-} polyanions form a stable three-dimensional framework, which provides safety under abusive conditions [16] and excellent cyclic performance. However, the strong covalent oxygen bonds also lead to low ionic diffusivity and poor electronic conductivity[17]. Thus, many efforts have been made to understand the transport properties of LFP and its derivatives. From the potential contributions to electronic transport in LFP and its derivatives, it is worth mentioning intrinsic carriers, which are describable in terms of wave packets and the electronic band structure with added time dependencies [18], and polaron hopping mechanisms, where the electron-phonon interaction has become too strong that the phonons (and electrons) cannot be considered independent quasiparticles anymore [19].

While the estimations within the framework of density functional theory (DFT) of the band gap vary widely, the low electronic conductivity of LFP was originally attributed to a large band gap and large effective mass of the Fe-3d electrons [16, 20, 21]. Although the exact value of band gap is still under debate [22-25], it is generally accepted that LFP is a wide band-gap material, which leads to a very small number of intrinsic charge carriers. Completely filled and completely empty bands, as appears to be the case for stoichiometric LFP, do not contribute to transport. All electric and thermal conductivity is to be attributed to partly filled bands [26]. In contrast, the small polaron conduction mechanism is considered to be the conduction mechanism in LFP, which is a thermally activated process and not

directly related to the band gap [22]. A series of experimental studies have been carried out to measure the activation energy of the electronic conductivity of LFP. A wide range of results were reported from 0.156 to 0.65 eV [20, 27-31], while the values obtained by first principle calculations are in the range of 0.185-0.22 eV for unconstrained polarons [32]. On the other hand, $FePO_4$ (FP) is believed to be a Mott insulator [33, 34].

Earlier studies on LFP found the presence of Li vacancies on the surface of LFP particles, while the core was well crystallized [35-37]. A more recent study on the solid-solution $Li_{0.5}FePO_4$ has shown that the Li migrates along the solid/liquid interface, without leaving the particle surfaces [38]. This mechanism takes place during both lithiation and de-lithiation, and it controls the phase transformation rate in Li_xFePO_4. As the surfaces of the electrode materials provide the interface to the electrolyte and the gateway for Li-ion transfer, they play an important role in the performance of LIBs[36] and their detailed characterization is receiving more focused research attention. As a matter of interest, the interfacial composition and structure between solid electrolytes and electrode materials often presents major deviations from those of the bulk materials too[38].

We have recently experimentally determined [25] that surface delithiation is characteristic in optimal quality LFP powders. The surface delithiation was equally observed in samples prepared by solution or hydrothermal methods. Although it is tempting to blame the delithiation on poor control of the lithium stoichiometry or due to loss of lithium during synthesis, this is very unlikely or impossible in the hydrothermal synthesis approach, which requires several molar excess of lithium and takes place at relatively low temperatures (< 200 °C). Therefore, the surface delithiation is more of an equilibrium characteristic of the synthesized nanoscale particles of LFP. This observation led to a re-evaluation of experimental measurements for the validation of electronic band structure calculations for LFP and FP, confirming the large band gap of stoichiometric LFP is about twice that of FP, and that thin nanometer scale surface layers of carbon and delithiation can effectively produce band gap edge shifts of several electron volts (eVs) having a significant influence in determined electronic properties.

From the above introduction, practical LFP materials consist of a relatively complex nanoscale architecture, not always considered in the analyses of their physical properties. Figure 1 shows a schematic of various nanoscale contributions that need to be considered for a more complete understanding of the electrical properties of practical LFP materials. Although the electrical conductivity of LFP at room or higher temperatures has been extensively investigated, the electrical

conduction at low cryogenic temperatures is also more poorly understood. In this work, we investigate the electrochemical, electrical and magnetic properties of LFP particularly at cryogenic temperatures, keeping in mind the potential roles and contributions of multiple nanoscale layers, which are part of the material, either by deliberate design or intrinsic equilibrium conditions.

2. Materials and Methods

2.1. Sample preparation

The LFP samples were prepared using a solution-based synthesis method. Oxalic acid dihydrate (≥99%, Sigma-Aldrich) and Ferrous oxalate dihydrate (99%, Sigma-Aldrich) were mixed in deionized water first. 30 wt. % H_2O_2 was slowly added into the mixture under magnetic stirring to dissolve Ferrous oxalate and form soluble Ferric oxalate. The temperature was controlled below 65 °C during this process to avoid the formation of iron oxide impurities.

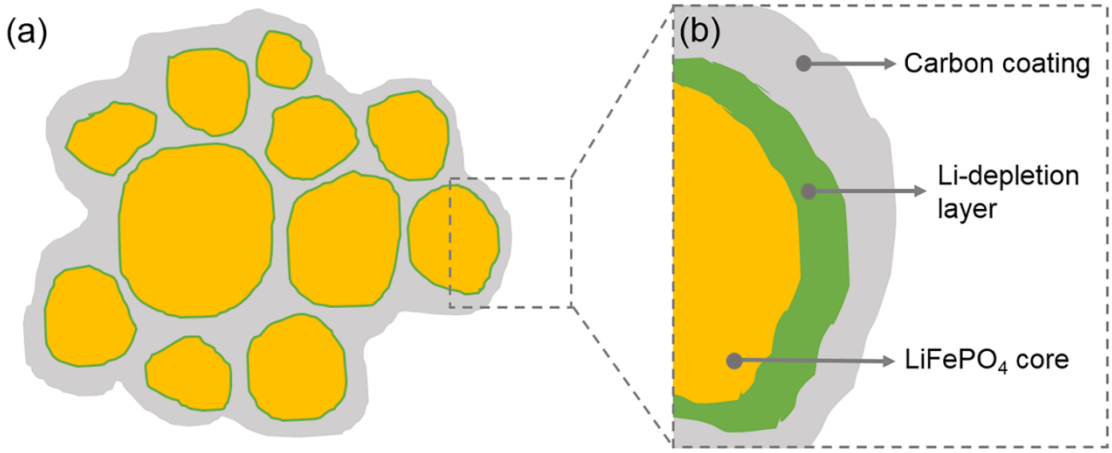

Figure 1. (a) Schematic of an agglomerated particle of carbon coated nanoscale particles of LFP material; (b) magnified view of an individual carbon coated LFP particle, where surface delithiation is also highlighted.

Stoichiometric amounts of Li_2CO_3 (≥ 99%, Sigma-Aldrich) and H_3PO_4 (85 wt. %) were added into the solution. 1 wt. % polyethylene glycol (PEG) was added to obtain nanoscale particles, as the amorphous carbon layer generated by organic carbon source could be coated on the LFP nano crystallites during pyrolysis, which prevented the grain size growth[39]. The resultant clear green solution was drawn into a vessel and reacted under vacuum. The resultant precursors were ring milled and calcined at 550 °C for 1 hour under argon atmosphere to form the LFP phase. The powder was bead milled, mixed with 8 wt. % sucrose, spray dried, and calcined in an argon atmosphere for conducting carbon coating at 710 °C for 1 hour (labelled as U710). The sample calcined at 710°C was subdivided

and portions were reheated at various higher temperatures in an argon atmosphere to investigate further temperature effects. The additional samples were labelled as U725 and U750 according to their calcination temperature (725 and 750 °C for 1 hour), respectively.

2.2. Structural Characterization

The structure and morphology of the samples were characterized by X-ray diffraction (XRD), scanning electron microscopy (SEM) and transmission electron microscopy (TEM). XRD was collected on a PANalytical X'Pert pro diffractometer with Co-K $_{\alpha}$ radiation, over a 2θ range between 15˚ and 90˚ with a 2θ step size of 0.017. The lattice parameters of the samples were refined with Rietveld refinement using Highscore Plus v4.8. The morphology and microstructure of the samples were investigated with a JEOL 7001 SEM and a JEOL 2100 TEM. Carbon analyses were conducted using a LECO TruMac CNS analyser. The furnace temperature for the carbon analyses was 1300 °C. The valence states on the surface of the samples were investigated with X-ray photoelectron spectroscopy (XPS, Kratos AXIS Supra photoelectron spectrometer) using a focused monochromated Al K $_{\alpha}$ radiation (hν = 1486.6 eV). The spectra were calibrated using the C 1s peak at 285.0 eV. Particle surface characteristics were also examined with Raman spectroscopy with a Renishaw inVia microscope equipped with a long working distance 50× objective lens and a 534 nm Ar $^{+}$ laser light source. As the decomposition of $LiFePO_4$ has been reported at a laser power of 1 mW[40], the laser power was controlled at 0.75 mW to avoid damaging the sample during measurement.

2.3. Conductivity and magnetic properties measurements

In order to gain more information on the electronic transport mechanism for carbon coated, surface delithiated LFP, the temperature dependence of the resistivity was investigated. One of the key questions was whether the behavior was more ohmic or temperature activated. The electrical conductivity and magnetic properties of the sample were measured with a mini cryogen-free magnet system (Cryogenic Limited). The powder samples were pressed into pellets with a diameter of 6 mm and thickness of ~1 mm. The applied pressure was determined by putting the sample powders into a press with a stainless-steel plunger and non-conductive hard plastic walls, as shown in the schematic in Figure S1(a). The change of the resistivity was monitored during pressing. As shown in Figure S1(b), a pressure of 2100 psi was determined when the resistivity stopped decreasing. The DC electrical resistivity of the samples was measured in the cryogenic equipment using a two-point configuration, because a four-point configuration resulted in resistance values that exceeded the maximum voltage compliance values of

the system. The two-point configuration also makes the measurement more dependent on the resistance of the connecting wires or cables. Data was collected in the temperature range of 5-295 K with the cryogenic system. External magnetic field (up to 0.5T) was also applied to study its effect on the electrical conductivity. The temperature dependences of the magnetic moment and magnetic susceptibility of the samples were measured by vibrating sample magnetometer (VSM) with an external magnetic field of 0 T and 0.5 T.

2.4. Electrochemical measurements

The electrochemical performance of the carbon coated LFP was evaluated by constructing a 2032 coin cell. The cathode slurry was prepared by mixing 90% LFP powder, 5% Super P, 5% PVDF and NMP solvent (99.5%, Sigma-Aldrich). The slurry was cast on carbon coated Al foil with the loading of 3 mg/cm^2. The 2032 coin cells were constructed with lithium foil as anode and 1 M $LiPF_6$ EC:DEC (1:1 by vol., Novolyte, BASF) electrolyte. Galvanostatic and cyclic voltammetry testing were carried out with a charge/discharge window between 2.5 V and 4.2 V utilizing a battery test system (BioLogic, VMP-300) at room temperature.

The electrochemical impedance of the as-prepared sample was determined by electrochemical impedance spectroscopy (EIS). The typical samples for EIS were pellets with a diameter of 6 mm and a thickness of ~3 mm. About 100 nm thick gold was deposited on both sides of the samples to serve as blocking electrodes avoiding the ionic exchange during the measurement. A sine wave signal in the frequency range from 5MHz to 1 mHz and amplitude of 5 mV was applied using the Biologic potentiostat.

3. Results and Discussion

3.1. Characterizations of sample U710

The XRD pattern of the U710 sample, together with the reference peak positions and Rietveld refinement fitting results, is shown in Figure 2(a). The pattern is entirely indexed as phase pure LFP with the space group Pnma. The average crystallite size calculated with Scherrer equation is 36±2 nm. Although the existence of antisite defect Fe_{Li} (Fe ions occupy Li site) has been confirmed previously[37, 41], the quality of the spectra is not sufficient to determine the presence of those defects. Therefore, only the lattice parameters have been refined by Rietveld refinement (shown in Table S1), which are in good agreement with previous literature [17].

SEM micrographs of the sample are shown in Figure 2(b). The primary particles are 100±50 nm and spherical secondary particles are formed with the application of spray-drying. The size distribution of the secondary particles is from several to more than ten micrometres, which is beneficial for tap density. The detailed microstructure of the sample is displayed on the TEM micrographs in Figure 3. The nanoscale primary particles are well crystallized and join an aggregate structure with an approximately uniformly distributed coating layer of carbon with a thickness of ~3 nm (see Figure 3(b)).

The Fe-2p high-resolution XPS has been carried out to get knowledge on the oxidation states of the particle surface. As shown in Figure 4(a), although no peaks of $FePO_4$ are detected in the XRD patterns, peaks of Fe $^{3+}$ 2p are found, indicating the existence of Fe^{3+} ions on the surface of the sample. The ratio of Fe $^{2+}$ and Fe^{3+} calculated from the peak area are shown in Figure 4(a). Surprisingly, around 50% of Fe ions on the surface are Fe^{3+}, even though carbon is supposed to be a protection layer to avoid oxidation. The presence of the large amount (~50 %) of Fe^{3+} suggests the presence of a Li-depletion layer around the particle in order to keep electrical neutrality. Similar Li-depletion layer has also been observed in carefully-prepared low carbon and hydrothermal LFP [25]. The Li might be expelled from the surface by reaction with carbon coating and/or oxidizing impurities, such as oxygen or water vapor, in the Ar atmosphere during synthesis. Moreover, the exposure to humid air has been reported resulting in the escape of Li from the surface due to the hydrophilic nature of Li [42]. These reactions would likely form hydroxide or carbonate like species, which largely maintain an amorphous nature, making them difficult to detect. The high quantity of C=C and C-C illustrated in C-1s XPS spectra (Figure 4(b)) and high ratio of G band and D band in Raman spectra (Figure 4(c)) indicates the high graphitization of the conducting carbon coating. The temperature dependence of the magnetic susceptibility of the sample with zero-field cooling (ZFC) and field cooling (FC) has been shown in Figure S2. A paramagnetic-antiferromagnetic transition has been found at 51 K (Néel temperature, T_N) with a Curie-Weiss behaviour above T_N, which is consistent with previous investigations [43, 44].

1

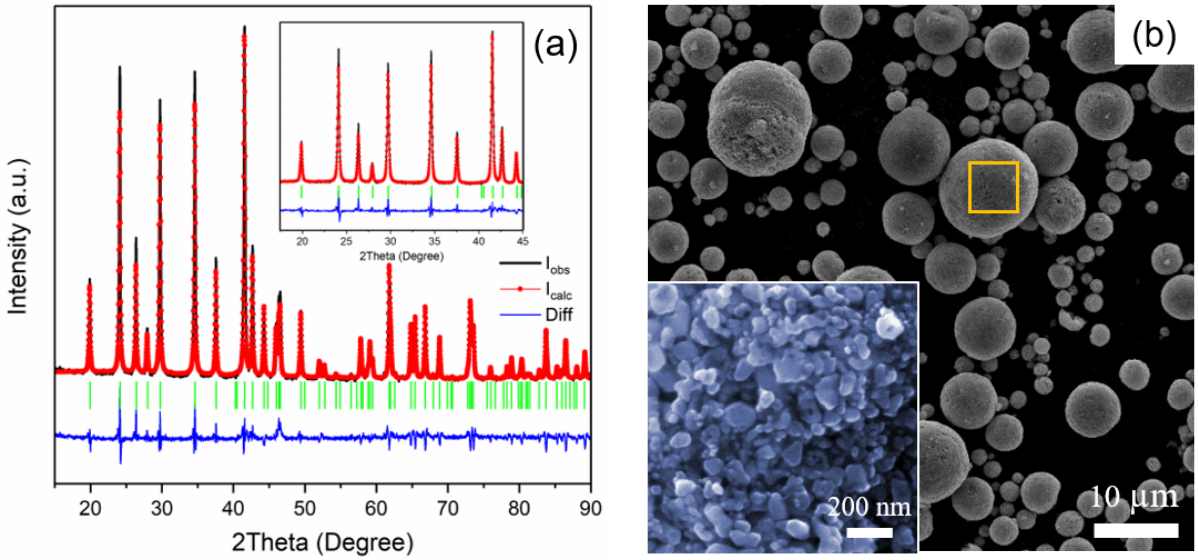

Figure 2. (a) XRD and Rietveld refinement (R_{Bragg}=1.78%, R_{wp}=3.37%, R_{exp}=2.47%) and (b) SEM micrographs for U710 sample.

2

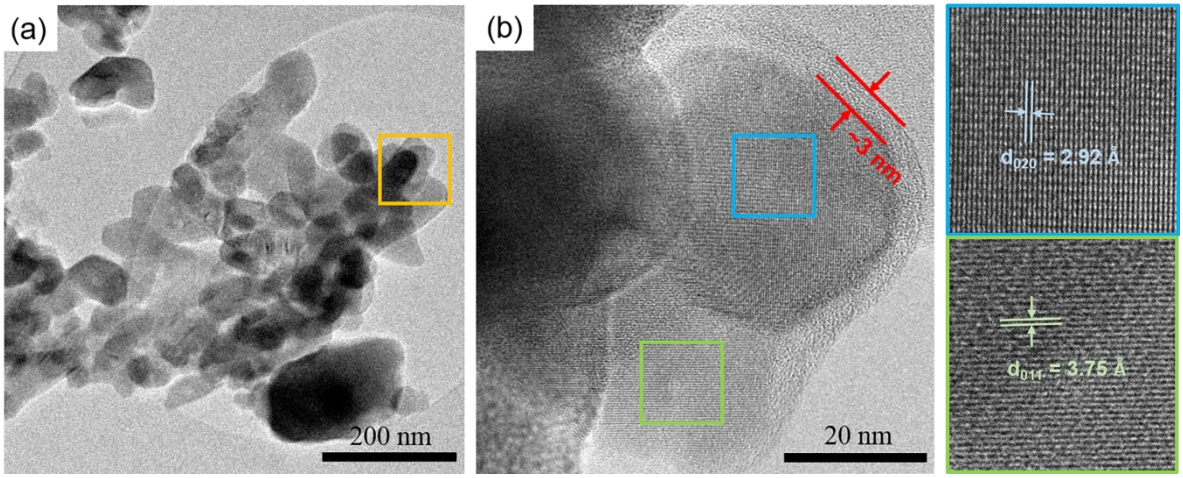

Figure 3. TEM micrographs for U710 sample. The detail TEM micrograph inside the yellow square in (a) is shown in (b). The insects on the right illustrate the high resolution TEM (HRTEM) images of the regions highlighted in (b) with corresponding colours.

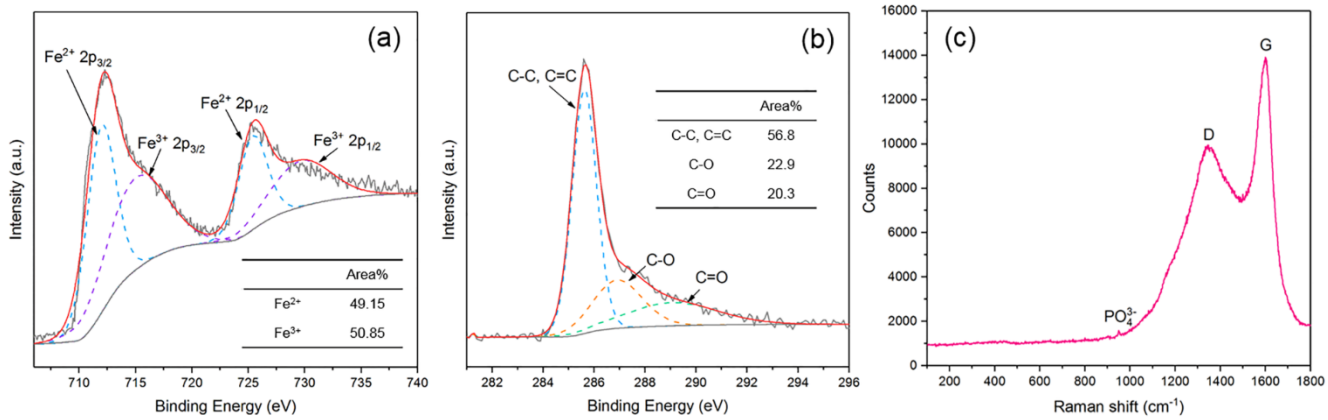

Figure 4 (a) Fe-2p and (b) C-1s high-resolution XPS spectra and (c) Raman spectrum for the synthesized $LiFePO_4$.

The electrochemical impedance of the U710 sample has been measured by EIS with the Au/LFP/Au cell. The Nyquist plot is displayed Figure 5. As the gold electrodes configuration blocks the lithium ions but is reversible for electronic exchange, the measured conduction is predominantly owing to the electronic carriers[30, 31]. The spectrum contains one large depressed semi-circle, however, a smaller one can also be seen in the magnified inset. According to the paper of Bauerle [45], the semi-circle at high frequency range and that at low frequency range can be assigned to the grain interior and the grain boundary, respectively. The resistivity caused by the grain boundary is two orders of magnitude higher than that caused by the grain interior, suggesting the grain boundary as the main obstruction for electron transport, even though the particles are carbon coated.

The Galvanostatic charge and discharge curves of the as-prepared LFP are illustrated in Figure 6. The voltage plateau close to 3.45 V at C/10 (1C=170mA/g) is a sign of the phase transition of $LiFePO_4$ and $FePO_4$ during charge and discharge[46]. The U710 sample shows a specific capacity of 150 mAh/g at C/10, which is close to the theoretical capacity (170mAh/g) and 123 mAh/g at 1C. The sample also shows a good rate performance with a capacity of 80 mAh/g at 15C charging and discharging. The electrochemical performance at high C- rate may be affected by the high internal resistance of coin cells.

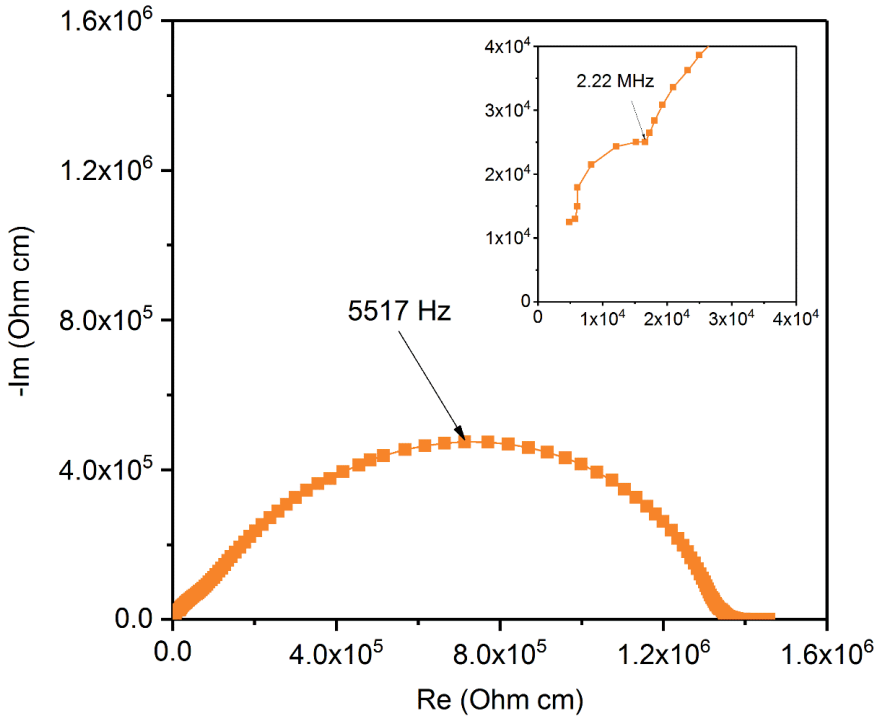

1

Figure 5. EIS spectra of U710 sample. The lines are added as a guide for eyes. The insect is the magnified EIS spectrum at high frequency range.

2

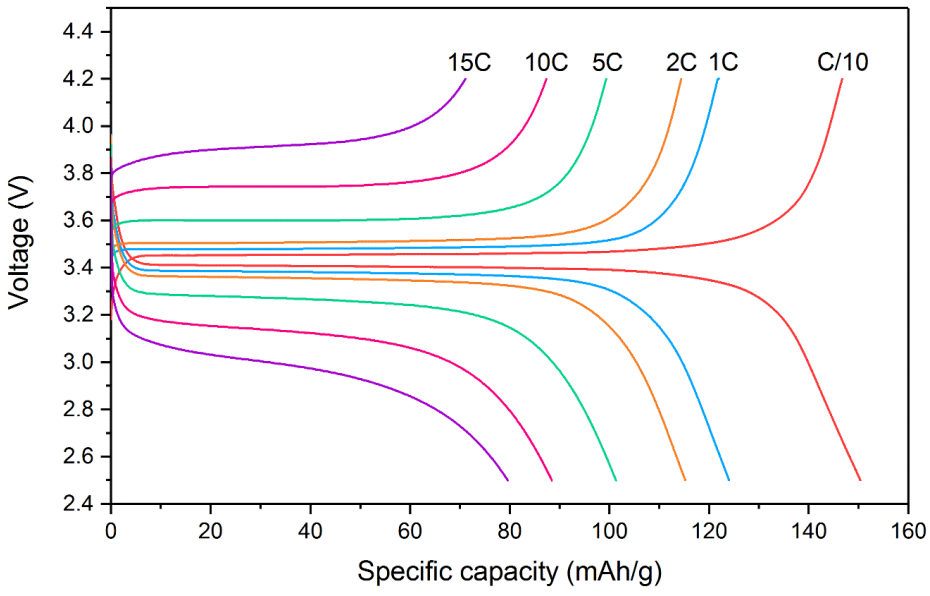

3

Figure 6. Galvanostatic Charge and discharge curves of as-prepared carbon coated $LiFePO_4$.

3.2 Temperature dependence of electrical resistivity

The electronic conductivity of LFP has been studied extensively in the range of -20~200 °C[28, 30, 47-51], which is or exceeds the working temperature range expected for batteries. The conductivity drop with the decrease of the temperature has been confirmed. In this study, the LFP sample has been cooled from room temperature to cryogenic temperatures with different applied currents. The changing trends of DC resistivity versus temperature from 295 to 20 K for the as-prepared carbon-coated LFP are illustrated in Figure 7. Interestingly, different behaviours have been found with different applied currents while the effect of the external magnetic field in the investigated range is negligible. The resistivity experiences abrupt changes from the smooth trend after the sample is cooled down from 295 to 110 K with applied current of 1×10^{-6} A. A minimum resistivity is achieved at 110 K. An increase of resistivity in the range of 110 to 30 K with a slope change at 50 K is observed followed by a sudden drop (11±0.5% based on the resistivity at room temperature) when the temperature is below 30 K. The sudden resistivity drop is also found in the low-carbon LFP sample carefully prepared in a previous study [25], as shown in the Figure S3. The resistivity increases back when the sample is heated back to 295 K with some fluctuation within 30-70 K and a local jump in resistivity above ~ 51K. Interestingly, the as-prepared sample shows a much simpler temperature dependence when the applied current increases to 1×10^{-4} A, as shown in Figure 7(b). The resistivity slightly increases within 295-250 K and decreases almost linearly within 250-30 K during cooling down, while the resistivity slightly drops within 25-50 K and increases linearly within 50-295 K during heating up.

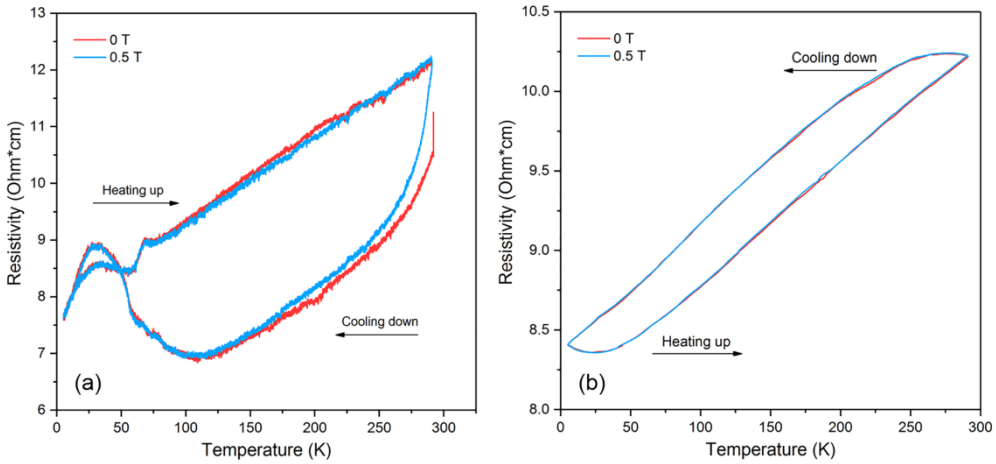

Figure 7. Temperature dependency of DC resistivity for as-prepared carbon-coated $LiFePO_4$ in the temperature range of 5~295 K with different applied currents of (a) 1×10^{-6} A and (b) 1×10^{-4} A.

As mentioned above, electron transport in LFP is usually considered to take place by small polaron migration. Electron delocalization was found in the solid-solution phase Li_xFePO_4 ($0<x<1$) and attributed to rapid small polaron hopping [52], which can be taken as evidence for a polaron conduction mechanism. The small polaron in LFP is also a magnetic polaron, as the moving t_{2g} electrons of Fe^{2+} carry with them a spin polarization cloud. Because of the strong localization of the charge carriers, the spin-polarization process was considered to not significantly affect the transport properties of LFP [23]. But in our investigation, as shown Figure 7a, several turning points from the smooth trend (110 and 30 K during cooling down, 30 K and 51K resistance jump during heating up) in the temperature dependency curves are close to T_N of LFP and even that of FP (125 K in reference[44], 100 K in this study as shown in Figure S4), indicating the conductivity of the composite LFP may be experiencing proximity effect to the magnetic configuration of the material. Due to the bandgap located between Fe-3d states, LFP and FP are classified as Mott insulators [53], which can host a surprisingly diverse set of quantum phenomena when their localized electrons are perturbed by various stimuli [54-56]. The small current, which is expected predominantly flowing across the carbon layer, appears to have a varied available cross section for transport, or modified resistance if the cross section remains constant, as the temperature is cooled below or heated above 51K. This suggests that the delithiated layer or other interfaces may have a temperature activated contribution to transport. When the applied current is higher, the effects on the conductivity of the magnetic configuration become negligible and no longer easily detectable by the measurements.

3.3 Effect of annealing temperature

The XRD patterns of the annealed samples, along with that of the original U710 sample, are compared in Figure 8. No impurity peaks, except those of pure olivine LFP, are detected after annealing at 725 °C for 1 h, while a small peak indicating the generation of schreibersite iron phosphide Fe_3P (JCPDS 00-064-0239) is observed in the spectrum for U750 (further supported by several peaks observed in the Raman spectra (see Figure 9)). As only one peak with low intensity for Fe_3P is identified in the spectrum, it is not sufficient for reliable quantitative analysis. Based on peak heights, it is estimated that the concentration of Fe_3P should be lower than 3%. The crystallite sizes calculated with the Scherrer equation are 42±3nm nm and 39±3 nm for U725 and U750 samples, respectively. The crystallite grew upon calcination. The smaller crystallite size of U750 may be caused by the decomposition at high temperature. Rietveld refinement has also been conducted to refine the lattice

parameters of the two calcined samples (as shown in Figure S5 and Table S1). There are no significant changes in the spherical morphology of the annealed samples according to the SEM micrograph, as illustrated in Figure S6. As expected, the carbon content decreases with the increase of calcination temperature. 2.67±0.05%, 2.09±0.05% and 1.96±0.05% of carbon have been measured for U710, U725 and U750, respectively. In a previous investigation, sample synthesis with Fe oxalate precursor, without adding additional carbon source, resulted in less than 1% carbon residue[25]. The sucrose is added after phase formation and bead milling, prior to spray drying and agglomeration, thus promoting a uniform distribution of the additional carbon coating around the particles. The XPS spectra for C-1s and Fe-2p of the three samples are illustrated in Figure S7. According to the peak area calculations, all the samples have high quality carbon coating with ~60 % of C=C and C-C, and the presence of Fe_3P does not have much effect on the redox states of Fe on the particle surfaces.

Raman spectroscopy has been carried out to get further knowledge on the phase purity of the annealed samples. As demonstrated in Figure 9, besides the bands corresponding to carbon (D band at ~1340 cm^{-1} and G band at ~1600 cm^{-1}) and PO_4^{3-} (at ~950 cm^{-1}), extra bands below 700 cm^{-1} are detected in both U725 and U750, indicating the existence of impurities, although no impurity peaks were detected using XRD for U725. The inability of XRD to detect Fe_3P peaks in U725 suggests the Fe_3P was below the detection limit (2% for in-lab XRD) or may alternatively be formed as an amorphous material on the surface.

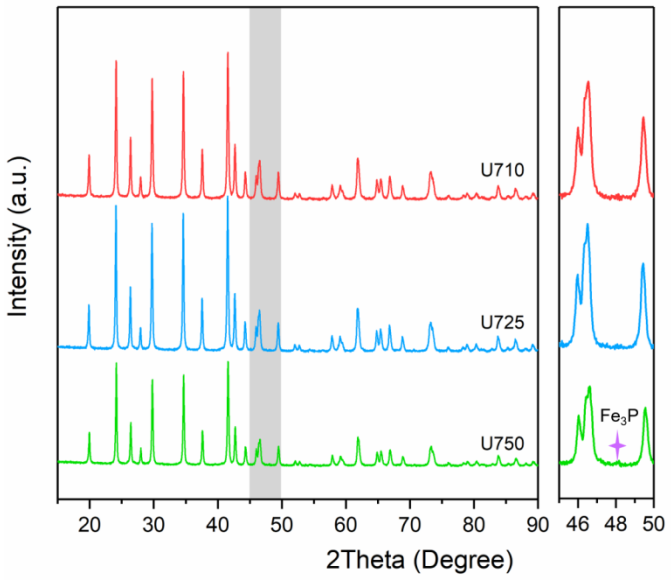

Figure 8. XRD spectra for the $LiFePO_4$ samples after annealing at different temperature for 1 hour.

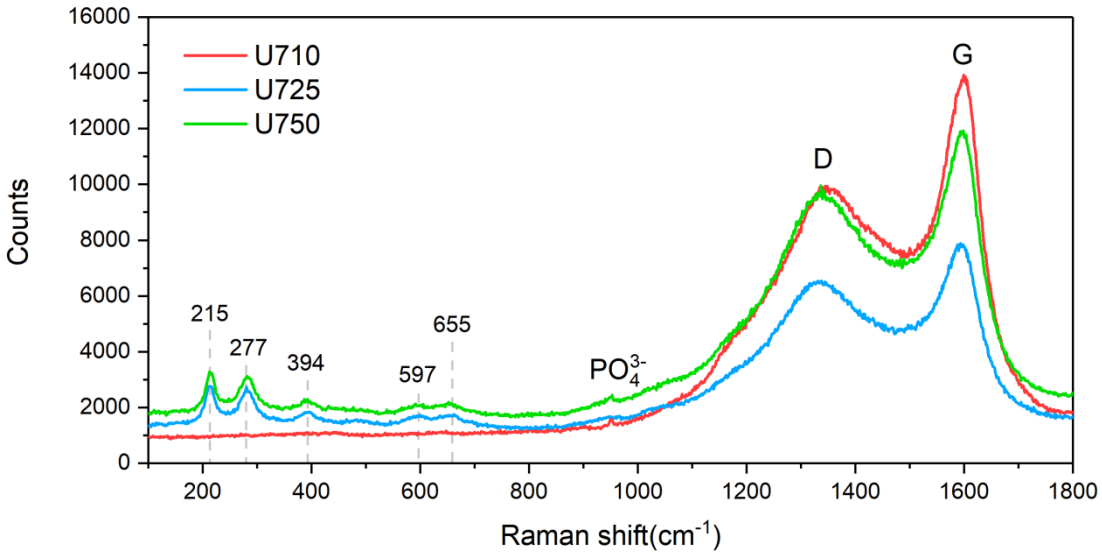

Figure 9. Raman spectra for the $LiFePO_4$ samples after annealing at different temperature for 1 hour.

All the extra bands marked in Figure 9 can be assigned to Fe_3P[57, 58], which is consistent with XRD results for U750. Therefore, LFP is slightly decomposed and Fe_3P is generated by reaction with the carbon in the system when the calcination temperature is higher than 710 °C. As sketched in Figure 1, the Li-depletion layer is in direct contact with the carbon coating, which makes it easier for these layers to react. The reaction between carbon and the Li-depletion layer could lead to oxidation of carbon to CO or CO_2, and reduction of PO_4 to form Fe_3P with the neighboring Fe [59].

As Fe_3P is a metallic conductor [60] and the poor rate performance of LFP is usually attributed to the low electronic conductivity of the material, the effect of this conductive impurity on the electrochemical performance of LFP electrode is worthy of investigation. However, an ambiguous influence was reported in previous literature[60-62]. The presence of FeP and Fe_2P along with Li_3PO_4 was assumed to lead to a significant rise in electronic conductivity of an LFP electrode by Rho et al[60]. That conclusion was then partially confirmed by a following study, where the sample that had more Fe_3P impurities showed better discharge capacity at all current densities tested [61]. In contrast, adverse effect was reported by Uchida et al [62], in which the sample with Fe_3P impurities exhibited less discharge capacity and poorer rate performance. Therefore, the electronic conductivity and electrochemical performance of the annealed samples are compared with those of the original U710 sample in this study.

The Nyquist plots of the samples are shown in Figure 10. Both of the annealed samples exhibit two semicircles nature, which is qualitatively (but not quantitatively) similar to the original U710 sample.

The existence of Fe_3P leads to a significant shrinking of the semicircle at the low frequency range, suggesting a drop of the bulk impedance by two orders of magnitude. The semicircle at the low frequency is almost halved after annealing, suggesting a half drop in boundary impedance. It appears that the existence of Fe_3P can improve the electronic conductivity of the material both in the interior of the grains and at the grain boundaries. However, a different story, one where the overall battery performance is deteriorated, is told by Galvanostatic charge-discharge measurements (see Figure 11).

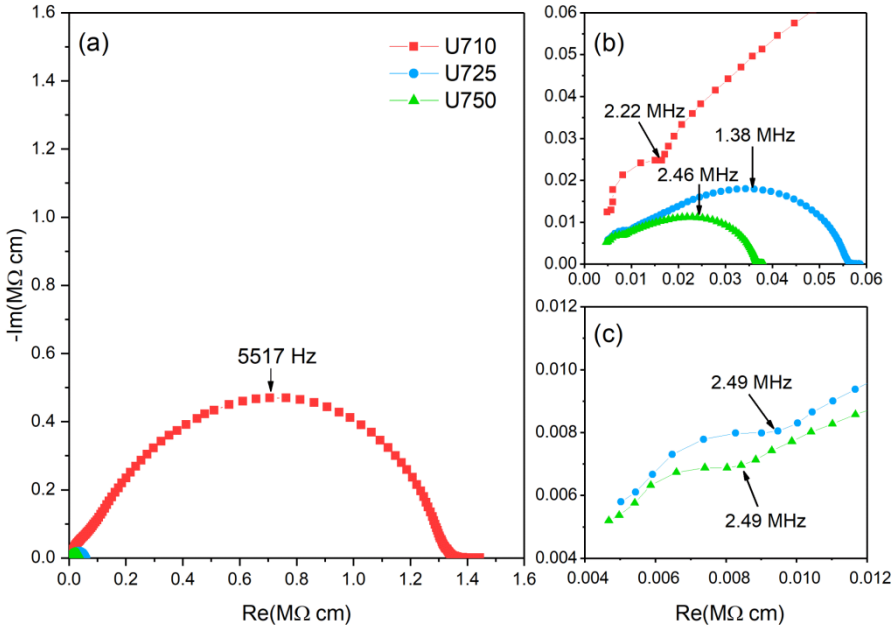

Figure 10. (a) EIS spectra for the LFP samples after annealing at different temperature for 1 hour. (b) and (c) are the partial magnification of the EIS spectra. The lines are the guide of eyes.

As shown in Figure 11, the annealed samples show lower charge and discharge capacity than that of U710 at C/10 and worse rate capability at 2C compared with U710. 4.5 mAh/g loss in capacity is expected with 3 wt.% loss of active materials (0.03×150 mAh/g). Therefore, the additional loss in capacity, especially for the U750 sample, cannot be simply explained by the loss of the active $LiFePO_4$. The detailed Galvanostatic charge and discharge curves of U725 and U750 samples at various C-rates are illustrated in Figure S8. The U725 sample shows similar charge and discharge capacity to U750, but relatively larger voltage differences between the charge and discharge plateaus at high C-rates. The relatively larger voltage plateau differences indicate more polarization. It is surprising that the significant enhancement in electronic conductivity has no positive effect on the electrochemical properties for LFP.

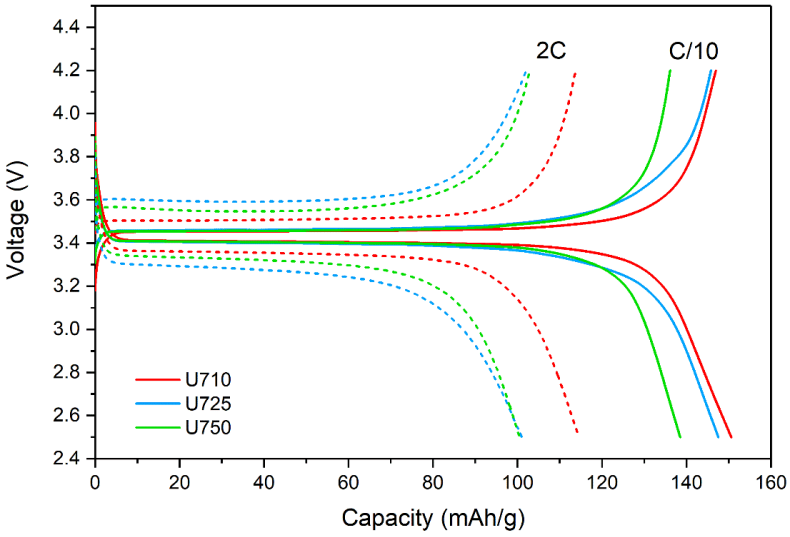

Figure 11. Galvanostatic Charge and discharge curves of $LiFePO_4$ samples after annealing.

To get further knowledge of the effect of the Fe_3P on the electrochemical behavior of LFP, cyclic voltammetry (CV) has been conducted at various scan rates of 0.1-3.2 mV/s between 2.5-4.5 V (vs. Li/Li^+). The CV curves at 0.1 mV/s are displayed in Figure 12(a). Relatively larger voltage differences between anodic and cathodic peaks are observed in U725 and U750 samples, which is consistent with the Galvanostatic test (Figure 11). The kinetic properties of lithium ions can be investigated using the peak currents at different scan rates. The chemical diffusion coefficient of Li-ion can be calculated using the relationship between the peak currents and the square root of the scan rates, which is based on the Randles-Sevcik equation[63]:

$$I_p = 0.4463F\left(\frac{F}{RT}\right)^{1/2} C_{Li} v^{1/2} A D_{Li}^{1/2},$$

where I_p is the peak current in amperes, F is Faraday constant (96485 C/mol), C_{Li} is the initial concentration of Li-ion (0.0228 mol/cm^3), R is the universal gas constant, v is the scan rate in V/s, A is the effective area of electrode in cm ^{2} (the area of the electrode is used in this study), and D_{Li} is the diffusion coefficient of Li-ion in cm^2/s. Accordingly, D_{Li} can be estimated by the slope of the peak currents as a function of square root of the scan rate. Although the equation originally describes the diffusion activity in solution, it is widely used to compare the Li diffusion in solid electrodes as the Li de/intercalation processes are considered as typical diffusion processes and can be modelled by a semi-infinite diffusion[64, 65]. The peak currents for both anodic and cathodic reaction of samples at each square root of the scan rate are presented in Figure 12(b). The linear fitting results and estimated D_{Li} are

shown in Table 1. The U710 sample has the highest D_{Li} for both anodic and cathodic reaction suggesting the presence of Fe_3P is detrimental, and may act as a surface barrier, for Li diffusion. It is worth noticing that U725 exhibits better electrochemical performance than U750 (as shown in Figure 11) even though both its electronic conductivity and Li diffusivity is lower than that of U750. The loss of the electrochemical performance may be caused by the side reactions due to the relatively larger amount of Fe_3P impurities, which is indicated by the shoulders before Fe^{2+}/Fe^{3+} redox couple in CV (Figure S9(c)).

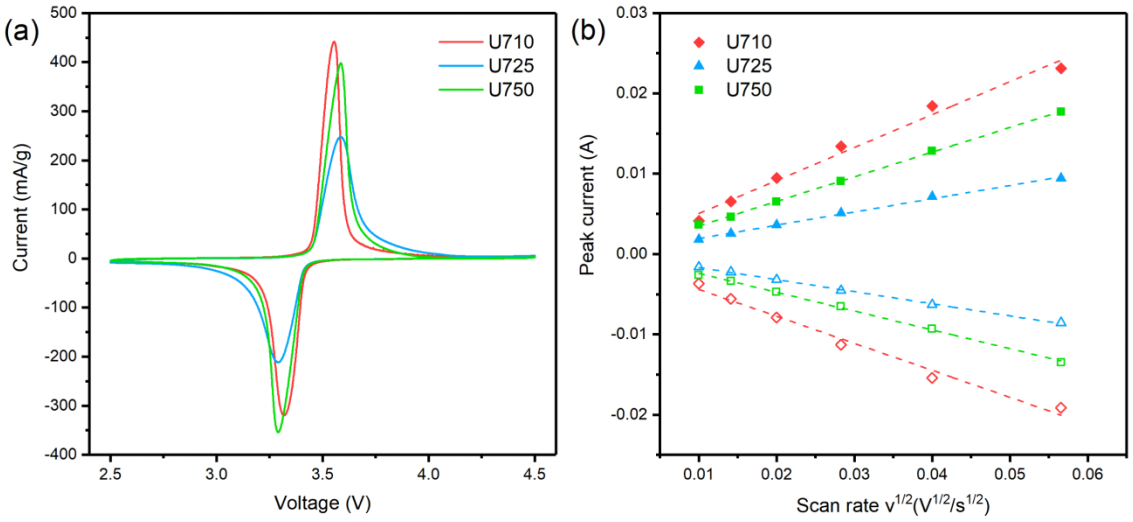

Figure 12. (a) Cyclic voltammetry and (b) peak currents as a function of square root of the scan rate for the LFP samples. The filled and hollow symbols represent the anodic and cathodic currents (I_a and I_c), respectively. The dash lines are the linear fitting results of the experimental results.

Table 1. The linear fitting results of the peak currents as a function of square root of the scan rate for the LFP samples and the calculated Li diffusion coefficient (D_{Li}).

		Slope	R^2	D_{Li} (cm^2/s)
U710	I_a	0.41003 ± 0.02543	0.98485	1.10×10^{-9}
	I_c	-0.33622 ± 0.02169	0.98363	7.43×10^{-10}
U725	I_a	0.1651 ± 0.00492	0.99646	1.79×10^{-10}
	I_c	-0.15043 ± 0.00284	0.99858	1.51×10^{-10}
U750	I_a	0.30674 ± 0.00304	0.99961	6.25×10^{-10}
	I_c	-0.23399 ± 0.00422	0.9987	3.56×10^{-10}

4. Conclusions

In summary, the electrochemical, electronic and magnetic properties of carbon coated $LiFePO_4$ samples have been investigated in significant detail and down to the cryogenic temperature range. The samples have been carefully prepared and show good electrochemical performance. The surfaces of the particles display complex nanostructures that influence the electrical, magnetic and electrochemical properties of the materials. Since the surfaces of the particles are the gateway that control the interaction of the cathode interface with the electrolyte, characterization of their nature is essential for adequate understanding of the overall battery material properties and design of next generation battery materials. An interesting temperature dependence and a sudden drop in the electrical resistance have been observed around the Néel temperature T_N of LFP and at low measuring currents, indicating proximity effect between the electronic and magnetic properties across the different layers of the nano-engineered LFP.

Furthermore, Fe_3P has been confirmed to precipitate on the particle surfaces when the carbon coated LFP is annealed beyond 710 °C. This metallic compound improves the electronic conductivity, but has adverse effect on the Li diffusivity, leading to worse electrochemical performance. This demonstrates that particle surface effects have a major role on overall battery performance and brings back the question as to what kind of surface we really need for a proper electrode material, which is worthy of further investigation for practical battery applications.

ASSOCIATED CONTENT

Electronic Supplementary Information (ESI) available: The detail of the pressure determination for pellet pressing, temperature dependency of magnetic susceptibility of $LiFePO_4$ and $FePO_4$, morphologies, high resolution XPS, Galvanostatic curves and cyclic voltammetry of the calcined samples. This material is available free of charge via the Internet at http://pubs.acs.org.

AUTHOR INFORMATION

Corresponding Author

* jose.alarco@qut.edu.au

Present Addresses

† Institute for Future Environments and Science and Engineering Faculty, Queensland University of Technology (QUT), Brisbane, QLD 4001 Australia.

Author Contributions

‡These authors contributed equally.

ACKNOWLEDGMENT

Yin Zhang would like to acknowledge CSIRO for the studentship, and the involvement of CRRC and the Rail Manufacturing Cooperative Research Centre (funded jointly by participating rail organisations and the Australian Federal Government's Cooperative Research Centres Program). The experimental data reported in this paper were obtained at the Central Analytical Research Facility operated by the Institute for Future Environments, Queensland University of Technology (QUT), Brisbane, Australia. Computational resources and services used in this work were provided by the HPC and Research Support Group, QUT. The authors would like to acknowledge Mr. Llew Rintoul, QUT, for the assistance with Raman spectroscopy, and Dr Mahboobeh Shahbazi, QUT, for the assistance with the magnetic property measurements.

REFERENCES

[1] A.K. Padhi, K. Nanjundaswamy, J.B. Goodenough, Phospho‐olivines as positive‐electrode materials for rechargeable lithium batteries, J. Electrochem. Soc., 144 (1997) 1188-1194.

[2] X.-C. Tang, L.-X. Li, Q.-L. Lai, X.-W. Song, L.-H. Jiang, Investigation on diffusion behavior of Li+ in LiFePO4 by capacity intermittent titration technique (CITT), Electrochim. Acta, 54 (2009) 2329-2334.

[3] Y. Liu, Y. Zhu, Y. Cui, Challenges and opportunities towards fast-charging battery materials, Nat. Energy, 4 (2019) 540–550.

[4] D.-H. Kim, J. Kim, Synthesis of LiFePO4 nanoparticles in polyol medium and their electrochemical properties, Electrochem. Solid-State Lett., 9 (2006) A439-A442.

[5] M.M. Doeff, J.D. Wilcox, R. Kostecki, G. Lau, Optimization of carbon coatings on LiFePO4, J. Power Sources, 163 (2006) 180-184.

[6] J. Li, L. Zhang, L. Zhang, W. Hao, H. Wang, Q. Qu, H. Zheng, In-situ growth of graphene decorations for high-performance LiFePO4 cathode through solid-state reaction, J. Power Sources, 249 (2014) 311-319.

[7] Z.-H. Wang, L.-X. Yuan, J. Ma, L. Qie, L.-L. Zhang, Y.-H. Huang, Electrochemical performance in Na-incorporated nonstoichiometric LiFePO 4/C composites with controllable impurity phases, Electrochim. Acta, 62 (2012) 416-423.

[8] A. Kulka, A. Braun, T.-W. Huang, A. Wolska, M.T. Klepka, A. Szewczyk, D. Baster, W. Zając, K. Świerczek, J. Molenda, Evidence for Al doping in lithium sublattice of LiFePO4, Solid State Ionics, 270 (2015) 33-38.

[9] Q. Zhang, S. Wang, Z. Zhou, G. Ma, W. Jiang, X. Guo, S. Zhao, Structural and electrochemical properties of Nd-doped LiFePO 4/C prepared without using inert gas, Solid State Ionics, 191 (2011) 40-44.

[10] I.V. Thorat, V. Mathur, J.N. Harb, D.R. Wheeler, Performance of carbon-fiber-containing LiFePO4 cathodes for high-power applications, J. Power Sources, 162 (2006) 673-678.

[11] P. Albertus, J. Christensen, J. Newman, Experiments on and modeling of positive electrodes with multiple active materials for lithium-ion batteries, J. Electrochem. Soc., 156 (2009) A606-A618.

[12] D. Wang, H. Li, S. Shi, X. Huang, L. Chen, Improving the rate performance of LiFePO4 by Fe-site doping, Electrochim. Acta, 50 (2005) 2955-2958.

[13] Y. Xu, Y. Lu, L. Yan, Z. Yang, R. Yang, Synthesis and effect of forming Fe2P phase on the physics and electrochemical properties of LiFePO4/C materials, J. Power Sources, 160 (2006) 570-576.

[14] M. Maccario, L. Croguennec, F. Weill, F. Lecras, C. Delmas, C-containing LiFePO4 materials — Part II: Electrochemical characterization, Solid State Ionics, 179 (2008) 2383-2389.

[15] S. Deng, H. Wang, H. Liu, J. Liu, H. Yan, Research progress in improving the rate performance of LiFePO4 cathode materials, Nano-Micro Lett., 6 (2014) 209–226.

[16] A. Yamada, S.-C. Chung, Crystal chemistry of the olivine-type Li(MnyFe1-y)PO4 and (MnyFe1-y)PO4 as Possible 4 V cathode materials for lithium batteries, J. Electrochem. Soc., 148 (2001) A960-A967.

[17] W.-J. Zhang, Structure and performance of LiFePO4 cathode materials: A review, Journal of Power Sources, 196 (2011) 2962-2970.

[18] H. Ibach, H. Lüth, Solid-state physics: an introduction to principles of material science, 2003.

[19] Y.M. Galperin, Introduction to modern solid state physics, CreateSpace Independent Publishing Platform, 2014.

[20] S. Shi, L. Liu, C. Ouyang, D.-s. Wang, Z. Wang, L. Chen, X. Huang, Enhancement of electronic conductivity of LiFePO4 by Cr doping and its identification by first-principles calculations, Phys. Rev. B, 68 (2003) 195108.
[21] P. Tang, N.A.W. Holzwarth, Electronic structure of FePO4,LiFePO4,and related materials, Phys. Rev. B, 68 (2003) 165107.
[22] F. Zhou, K. Kang, T. Maxisch, G. Ceder, D. Morgan, The electronic structure and band gap of LiFePO4 and LiMnPO4, Solid State Commun., 132 (2004) 181-186.
[23] K. Zaghib, A. Mauger, J.B. Goodenough, F. Gendron, C. Julien, Electronic, optical, and magnetic properties of LiFePO4: small magnetic polaron effects, Chem. Mater., 19 (2007) 3740-3747.
[24] S. Furutsuki, S.-C. Chung, S.-i. Nishimura, Y. Kudo, K. Yamashita, A. Yamada, Electrochromism of LixFePO4 induced by intervalence charge transfer transition, J. Phys. Chem. C, 116 (2012) 15259-15264.
[25] Y. Zhang, J.A. Alarco, A.S. Best, G.A. Snook, P.C. Talbot, J.Y. Nerkar, Re-evaluation of experimental measurements for the validation of electronic band structure calculations for LiFePO4 and FePO4, RSC Adv., 9 (2019) 1134-1146.
[26] N. Manini, Introduction to the Physics of Matter: Basic atomic, molecular, and solid-state physics, Springer, 2015.
[27] M. Takahashi, S.-i. Tobishima, K. Takei, Y. Sakurai, Reaction behavior of LiFePO4 as a cathode material for rechargeable lithium batteries, Solid State Ionics, 148 (2002) 283-289.
[28] Y.-N. Xu, S.-Y. Chung, J.T. Bloking, Y.-M. Chiang, W.Y. Ching, Electronic structure and electrical conductivity of undoped LiFePO4, Electrochem. Solid-State Lett., 7 (2004) A131-A134.
[29] C. Delacourt, C. Wurm, L. Laffont, J.B. Leriche, C. Masquelier, Electrochemical and electrical properties of Nb- and/or C-containing LiFePO4 composites, Solid State Ionics, 177 (2006) 333-341.
[30] R. Amin, P. Balaya, J. Maier, Anisotropy of Electronic and Ionic Transport in LiFePO4 Single Crystals, Electrochem. Solid-State Lett., 10 (2007) A13-A16.
[31] R. Amin, Effect of annealing on transport properties of LiFePO4: Towards a defect chemical model, Solid State Ionics, 178 (2008) 1831-1836.
[32] T. Maxisch, F. Zhou, G. Ceder, Ab initio study of the migration of small polarons in olivine LixFePO 4 and their association with lithium ions and vacancies, Phys. Rev. B, 73 (2006) 104301.
[33] L. Craco, S. Leoni, Electrodynamics and quantum capacity of LixFePO4 battery material, Appl. Phys. Lett., 99 (2011) 192103.
[34] L. Craco, S. Leoni, Electron localization in olivine materials for advanced lithium-ion batteries, J. Appl. Phys., 111 (2012) 112602.
[35] K. Zaghib, A. Mauger, F. Gendron, C.M. Julien, Surface Effects on the Physical and Electrochemical Properties of Thin LiFePO4Particles, Chem. Mater., 20 (2008) 462-469.
[36] P. Benedek, N. Yazdani, H. Chen, N. Wenzler, F. Juranyi, M. Månsson, M.S. Islam, V.C. Wood, Surface phonons of lithium ion battery active materials, Sustain. Energy Fuels, 3 (2019) 508-513.
[37] T. Famprikis, P. Canepa, J.A. Dawson, M.S. Islam, C. Masquelier, Fundamentals of inorganic solid-state electrolytes for batteries, Nat. Mater., 18 (2019) 1278–1291.
[38] Y. Li, H. Chen, K. Lim, H.D. Deng, J. Lim, D. Fraggedakis, P.M. Attia, S.C. Lee, N. Jin, J. Moskon, Z. Guan, W.E. Gent, J. Hong, Y.S. Yu, M. Gaberscek, M.S. Islam, M.Z. Bazant, W.C. Chueh, Fluid-enhanced surface diffusion controls intraparticle phase transformations, Nat. Mater., 17 (2018) 915-922.
[39] Q.-B. Liu, S.-J. Liao, H.-Y. Song, Z.-X. Liang, High-performance LiFePO4/C materials: Effect of carbon source on microstructure and performance, J. Power Sources, 211 (2012) 52-58.
[40] E. Markevich, R. Sharabi, O. Haik, V. Borgel, G. Salitra, D. Aurbach, G. Semrau, M. Schmidt, N. Schall, C. Stinner, Raman spectroscopy of carbon-coated LiCoPO4 and LiFePO4 olivines, J. Power Sources, 196 (2011) 6433-6439.
[41] K. Hoang, M. Johannes, Tailoring native defects in LiFePO4: insights from first-principles calculations, Chem. Mater., 23 (2011) 3003-3013.
[42] K. Zaghib, M. Dontigny, P. Charest, J. Labrecque, A. Guerfi, M. Kopec, A. Mauger, F. Gendron, C. Julien, Aging of LiFePO4 upon exposure to H2O, J. Power Sources, 185 (2008) 698-710.
[43] C.M. Julien, A. Ait-Salah, A. Mauger, F. Gendron, Magnetic properties of lithium intercalation compounds, Ionics, 12 (2006) 21-32.
[44] G. Rousse, J. Rodriguez-Carvajal, S. Patoux, C. Masquelier, Magnetic structures of the triphylite LiFePO4 and of its delithiated form FePO4, Chem. Mater., 15 (2003) 4082-4090.
[45] J. Bauerle, Study of solid electrolyte polarization by a complex admittance method, J. Phys. Chem. Solids, 30 (1969) 2657-2670.
[46] Z. Xu, L. Gao, Y. Liu, L. Li, Review—Recent developments in the doped LiFePO4 cathode materials for power lithium ion batteries, J. Electrochem. Soc., 163 (2016) A2600-A2610.
[47] S.Y. Chung, J.T. Bloking, Y.M. Chiang, Electronically conductive phospho-olivines as lithium storage electrodes, Nat. Mater., 1 (2002) 123-128.
[48] S.-Y. Chung, Y.-M. Chiang, Microscale measurements of the electrical conductivity of doped LiFePO4, Electrochem. Solid-State Lett., 6 (2003) A278-A281.
[49] S.J. Kwon, C.W. Kim, W.T. Jeong, K.S. Lee, Synthesis and electrochemical properties of olivine LiFePO4 as a cathode material prepared by mechanical alloying, J. Power Sources, 137 (2004) 93-99.
[50] W.-b. Luo, L. Wen, H.-z. Luo, R.-s. Song, Y.-c. Zhai, C. Liu, F. Li, Carbon nanotube-modified LiFePO4 for high rate lithium ion batteries, New Carbon Mater., 29 (2014) 287-294.
[51] F. Wang, J. Chen, Z. Tan, M. Wu, B. Yi, W. Su, Z. Wei, S. Liu, Low-temperature electrochemical performances of LiFePO4 cathode materials for lithium ion batteries, J. Taiwan Imst. Chem. E., 45 (2014) 1321-1330.
[52] B. Ellis, L.K. Perry, D.H. Ryan, L. Nazar, Small polaron hopping in LixFePO4 solid solutions: coupled lithium-ion and electron mobility, J. Am. Chem. Soc., 128 (2006) 11416-11422.
[53] Y.-N. Xu, W.Y. Ching, Y.-M. Chiang, Comparative studies of the electronic structure of LiFePO4, FePO4, Li3PO4, LiMnPO4, LiCoPO4, and LiNiPO4, J. Appl. Phys., 95 (2004) 6583-6585.

[54] A. Camjayi, C. Acha, R. Weht, M. Rodríguez, B. Corraze, E. Janod, L. Cario, M. Rozenberg, First-order insulator-to-metal Mott transition in the paramagnetic 3D System GaTa4Se8, Phys. Rev. Lett., 113 (2014) 086404.
[55] M. Rozenberg, G. Kotliar, H. Kajueter, G. Thomas, D. Rapkine, J. Honig, P. Metcalf, Optical conductivity in Mott-Hubbard systems, Phys. Rev. Lett., 75 (1995) 105.
[56] M. Imada, A. Fujimori, Y. Tokura, Metal-insulator transitions, Rev. Mod. Phys., 70 (1998) 1039-1263.
[57] C. Pirim, M. Pasek, D. Sokolov, A. Sidorov, R. Gann, T. Orlando, Investigation of schreibersite and intrinsic oxidation products from Sikhote-Alin, Seymchan, and Odessa meteorites and Fe3P and Fe2NiP synthetic surrogates, Geochim. Cosmochim. Acta, 140 (2014) 259-274.
[58] M. Kaliwoda, R. Hochleitner, V.H. Hoffmann, T. Mikouchi, A.M. Gigler, W.W. Schmahl, New Raman spectroscopic data of the almahata sitta meteorite, Spectrosc. Lett., 46 (2013) 141-146.
[59] B. Ellis, P.S. Herle, Y.-H. Rho, L. Nazar, R. Dunlap, L.K. Perry, D. Ryan, Nanostructured materials for lithium-ion batteries: Surface conductivity vs. bulk ion/electron transport, Faraday Discuss., 134 (2007) 119-141.
[60] Y.-H. Rho, L.F. Nazar, L. Perry, D. Ryan, Surface chemistry of LiFePO4 studied by Mössbauer and X-ray photoelectron spectroscopy and its effect on electrochemical properties, J. Electrochem. Soc., 154 (2007) A283-A289.
[61] E. Ershenko, A. Bobyl, M. Boiko, Y. Zubavichus, V. Runov, M. Trenikhin, M. Sharkov, Fe3P impurity phase in high-quality LiFePO4: X-ray diffraction and neutron-graphical studies, Ionics, 23 (2017) 2293-2300.
[62] S. Uchida, M. Yamagata, M. Ishikawa, Novel rapid synthesis method of LiFePO4/C cathode material by high-frequency induction heating, J. Power Sources, 243 (2013) 481-487.
[63] A.J. Bard, L.R. Faulkner, Electrochemical methods: fundamentals and applications, 1980.
[64] A.J. Bard, L.R. Faulkner, Electrochemical Methods, 1980.
[65] Y. Denis, C. Fietzek, W. Weydanz, K. Donoue, T. Inoue, H. Kurokawa, S. Fujitani, Study of LiFePO4 by cyclic voltammetry, J. Electrochem. Soc., 154 (2007) A253-A257.

Declaration of interests

☒ The authors declare that they have no known competing financial interests or personal relationships that could have appeared to influence the work reported in this paper.

☐The authors declare the following financial interests/personal relationships which may be considered as potential competing interests:

In this study, we have investigated electrical and magnetic properties of LFP down to cryogenic temperatures. An electronic resistivity drop was observed when the temperature was below the Néel temperature at low applied currents, indicating a likely interaction between the magnetic configuration of the core LFP and electronic transport mechanisms. Metallic Fe_3P was precipitated on the samples surfaces after annealing at high temperature in Argon. The existence of Fe_3P was found to significantly improve the electronic conductivity but it took a toll on the electrochemical performance.

Nanoscale characteristics of practical $LiFePO_4$ materials - effects on electrical, magnetic and electrochemical properties

Yin Zhang [1, 2, 4], Jose A. Alarco [1,*], Jawahar Y. Nerkar [1], Adam S. Best [2], Graeme A. Snook [3], and Peter C. Talbot [1]

[1]Institute for Future Environments and Science and Engineering Faculty, Queensland University of Technology (QUT), Brisbane, QLD 4001 Australia

[2]CSIRO Manufacturing, Private Bag 10, Clayton South, Victoria 3169, Australia

[3]CSIRO Mineral Resources, Private Bag 10, Clayton South, Victoria 3169, Australia

[4]CRRC Qingdao Sifang Rolling Stock Research Institute Co., Ltd., Qingdao 266031, China

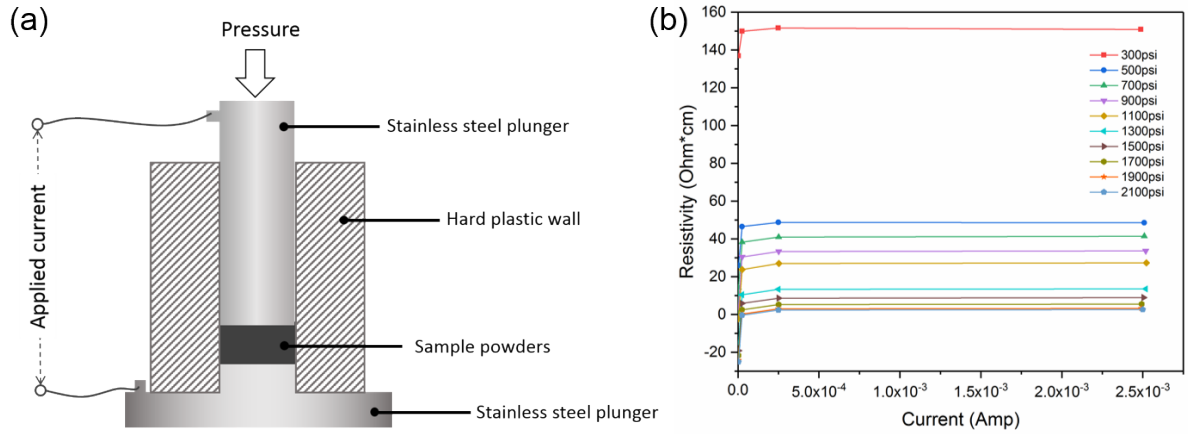

Figure S1 (a) Schematic of the apparatus for determination of the pressure. (b) The DC resistivity of U750 sample under different pressures. Notice a negative recorded resistance at low currents, which appears related to inductive effects[1] from the core-shell nano-layered structure of the material particles

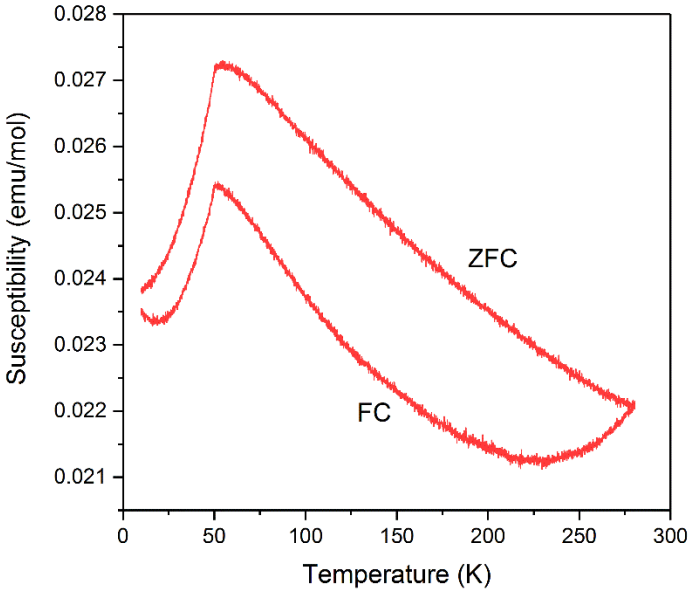

Figure S2 Temperature dependency of molar magnetic susceptibility of the $LiFePO_4$ sample with zero-field cooling (ZFC) and field cooling (FC) at 0.5 T.

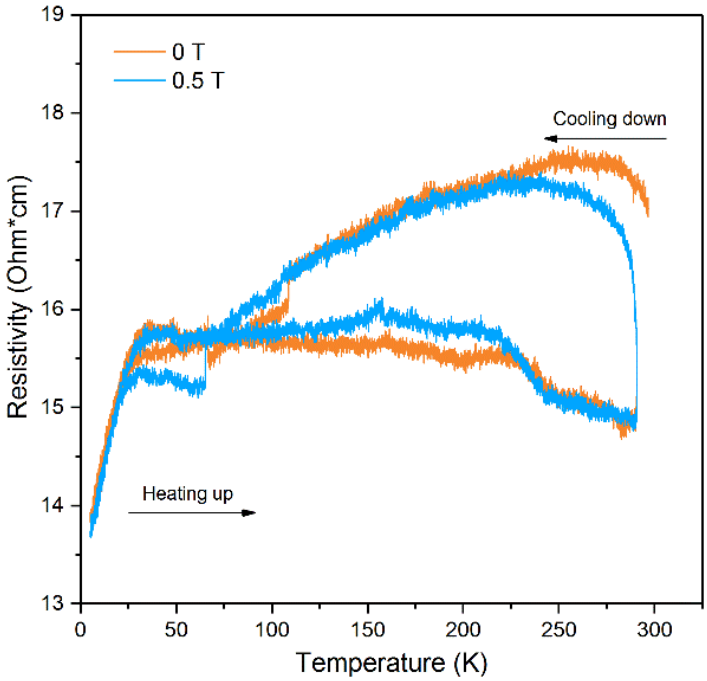

Figure S3 DC resistivity for low-carbon $LiFePO_4$ samples used in previous investigation[2] in the temperature range of 5~295 K with applied current of 1×10^{-6} A.

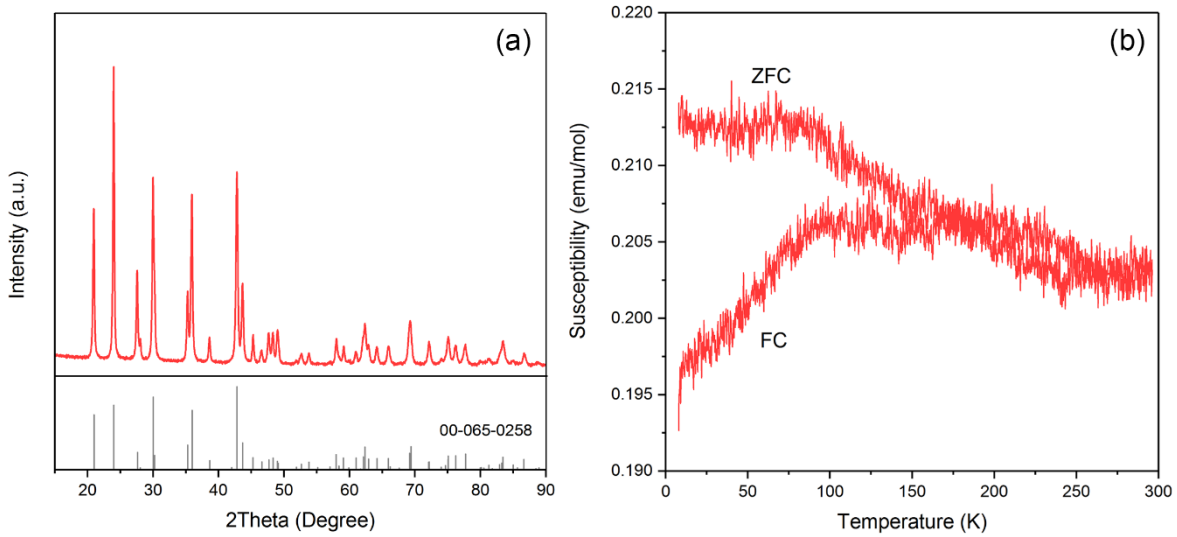

Figure S4 (a) XRD pattern of the delithiated sample and the reference $FePO_4$ peaks, indicating pure $FePO_4$ was obtained. (b) Temperature dependency of molar magnetic susceptibility of $FePO_4$ with ZFC and FC at 0.05 T. A paramagnetic-antiferromagnetic transition has been found at 100 K, which is lower than that in previous literature (125 K[3]).The $FePO_4$ samples were obtained by chemical delithiation of U710 samples with the method reported in reference[2].

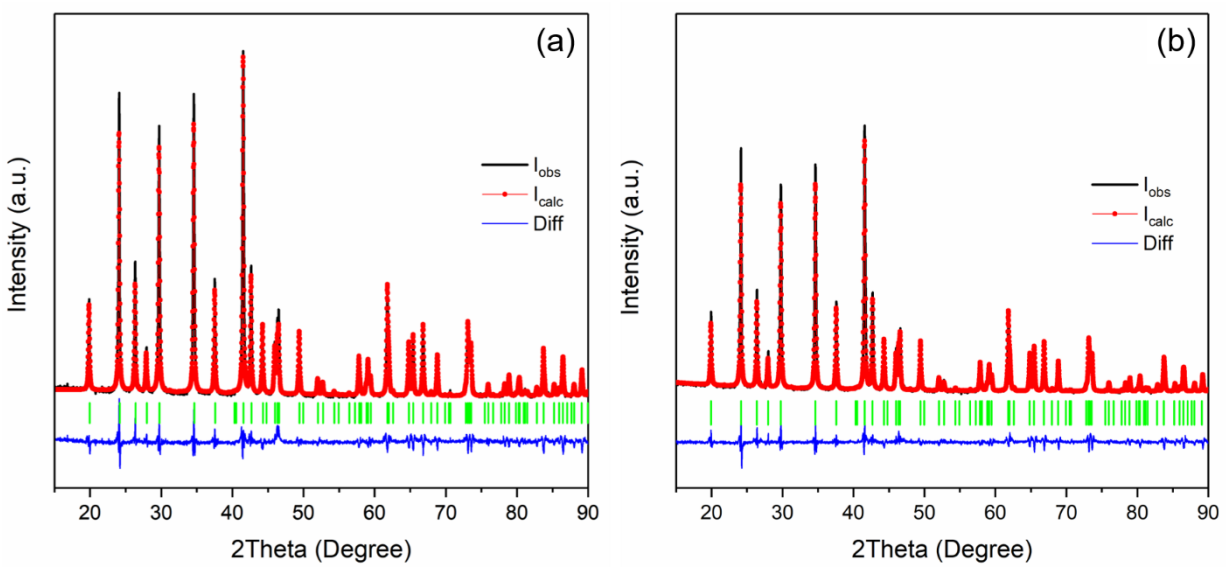

Figure S 5 XRD and Rietveld refinement for (a) U725 and (b) U750 samples.

Table S1 Rietveld refinement results for the LFP samples.

	U710	U725	U750
a/Å	10.3206(1)	10.3221(1)	10.3187(1)
b/Å	6.00239(8)	6.00323(7)	6.00164(8)
c/Å	4.69241(7)	4.69197(6)	4.69228(6)
α/°	90	90	90
β/°	90	90	90
γ/°	90	90	90
Cell volume/ $Å^3$	290.6883	290.7426	290.5901
R_{wp}/%	3.37	3.39	4.55
R_{exp}/%	2.47	3.01	3.38
R_{Bragg}/%	1.78	1.73	1.71

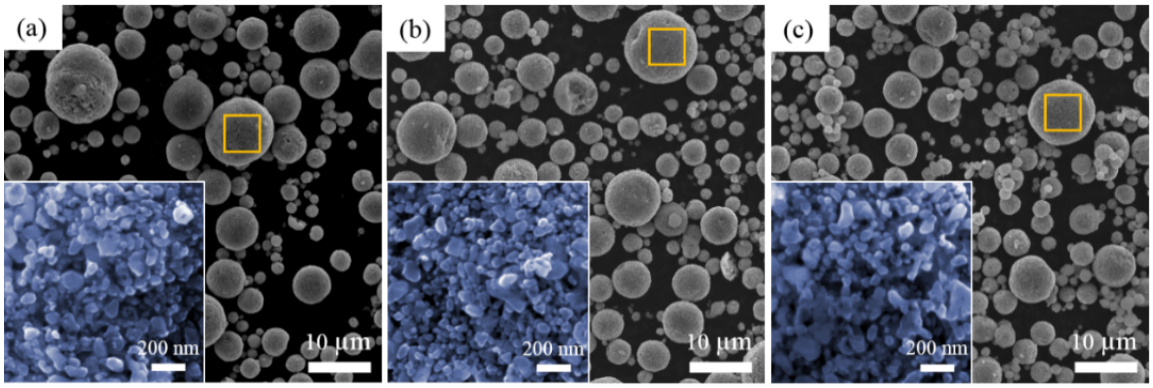

Figure S6 SEM micrographs for (a) U710, (b) U725 and (c) U750. The insects are the magnifications of the parts marked with the yellow square.

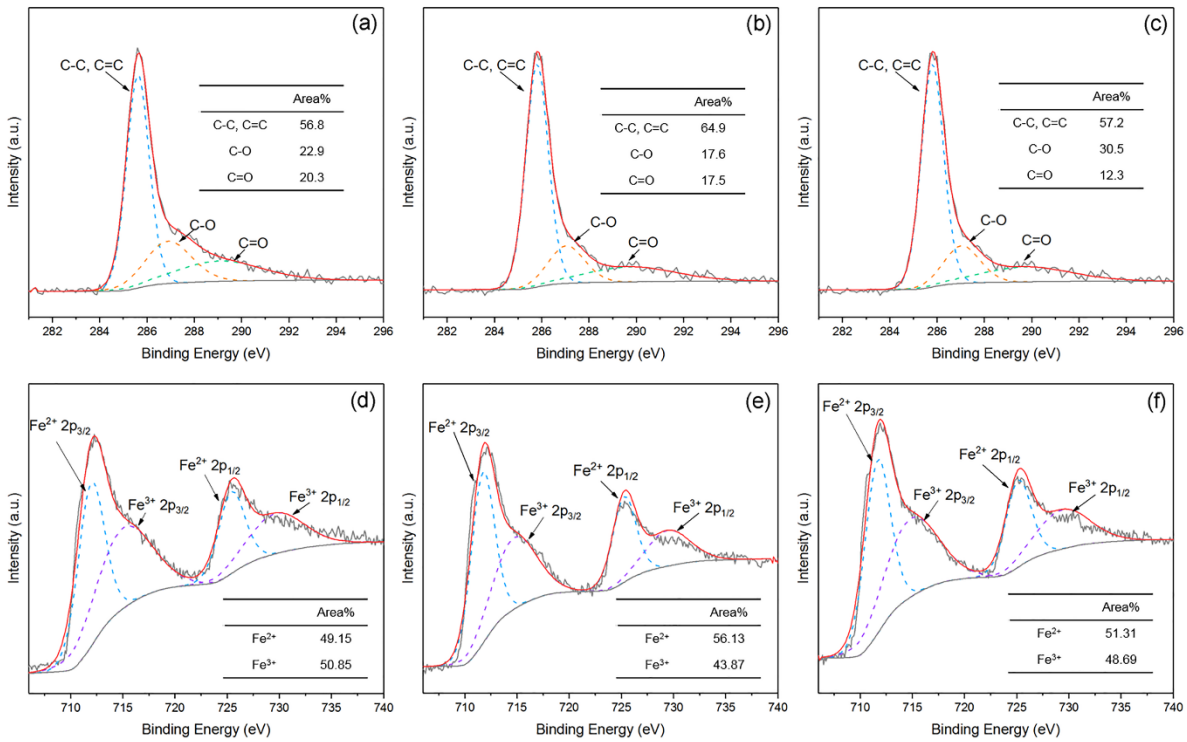

Figure S7 C-1s and Fe-2p high resolution XPS spectra for (a, d) U710, (b, e) U725, and (c, f) U750.

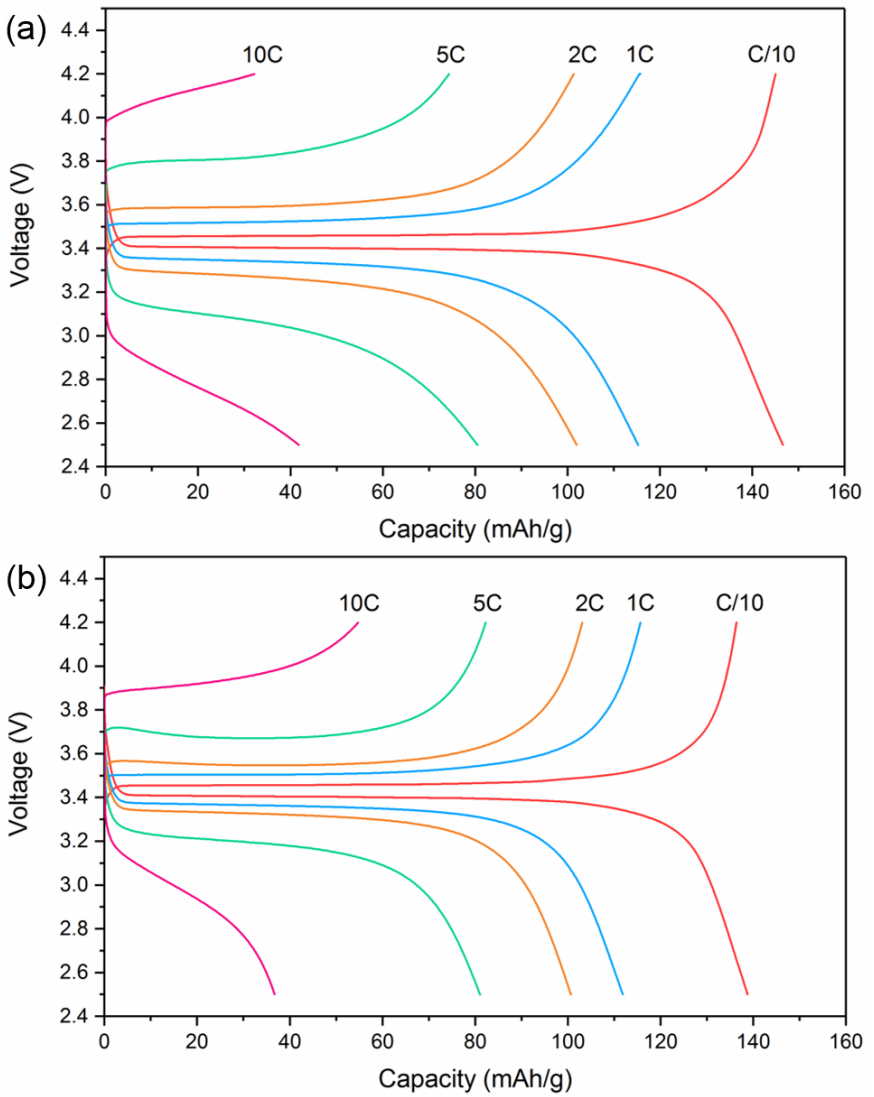

Figure S8 Galvanostatic Charge and discharge curves of (a) U725 and (b) U750 sample.

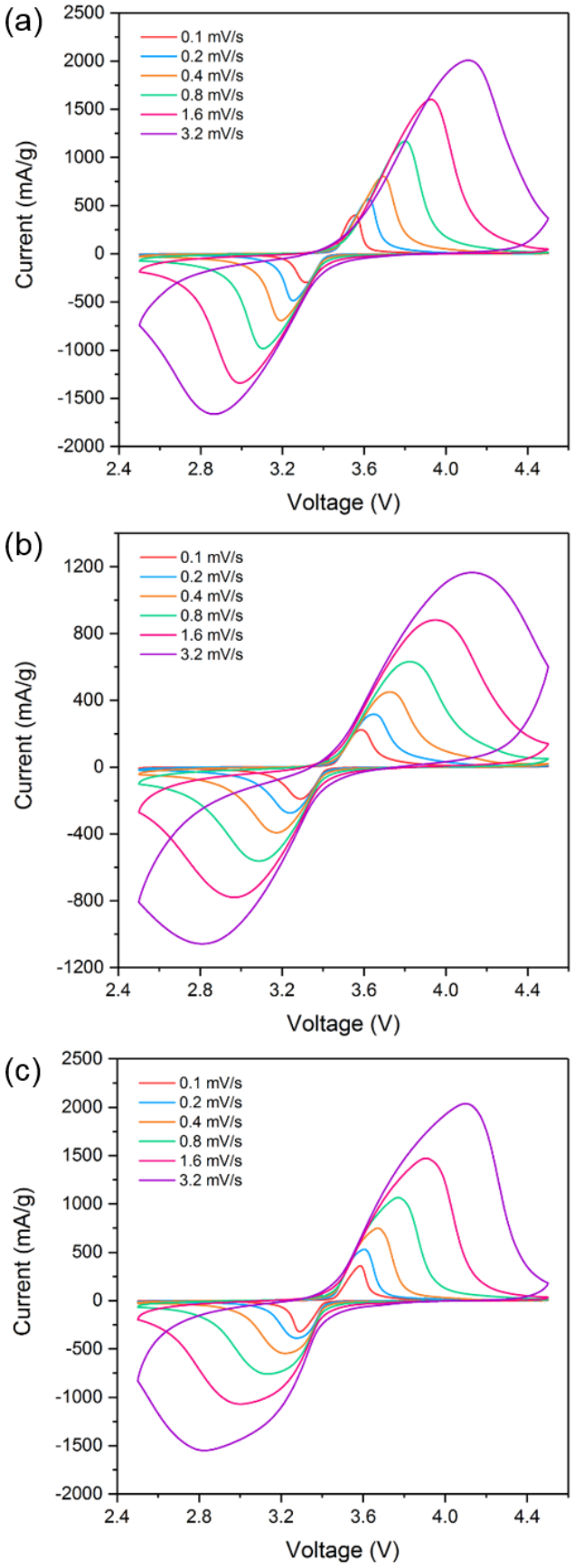

Figure S9 Cyclic voltammetry of (a) U710, (b) U725 and (c) U750 at various scan rates of 0.1-3.2 mV/s between 2.5-4.5 V (vs. Li/Li$^+$).

References

1. Jorritsma, J. and J. Mydosh, *Anomalous negative resistance in superconducting vanadium nanowires.* Physical Review B, 2000. **62**(14): p. 9703.
2. Zhang, Y., J.A. Alarco, A.S. Best, G.A. Snook, P.C. Talbot, and J.Y. Nerkar, *Re-evaluation of experimental measurements for the validation of electronic band structure calculations for LiFePO4 and FePO4.* RSC Advances, 2019. **9**(2): p. 1134-1146.
3. Rousse, G., J. Rodriguez-Carvajal, S. Patoux, and C. Masquelier, *Magnetic structures of the triphylite LiFePO4 and of its delithiated form FePO4.* Chemistry of materials, 2003. **15**(21): p. 4082-4090.